Simple method for the assessment of intrinsic kinetic constants in photocatalytic microreactors

M.L. Satuf[a,*], J. Macagno[a], A. Manassero[a], G. Bernal[b], P.A. Kler[b,c], C.L.A. Berli[a]

[a] *Instituto de Desarrollo Tecnológico para la Industria Química (INTEC, UNL-CONICET), Colectora RN 168 Km 472, Santa Fe, Argentina*
[b] *Departamento de Ingeniería en Sistemas de Información, FRSF-UTN. Lavaise 610, Santa Fe, Argentina*
[c] *Centro de Investigación de Métodos Computacionales (CIMEC, UNL-CONICET), Colectora RN 168 Km 472, Santa Fe, Argentina*

A B S T R A C T

A simple method for obtaining intrinsic kinetic parameters of photocatalytic, first-order reactions is presented. The method makes use of a microfluidic reactor, which was specifically designed to operate under conditions of negligible mass transfer limitations and involves a reversible sealing that allows one to test different catalyst films on the same device. An analytical model was derived to calculate the intrinsic kinetic constant from experimental data of reactant conversion vs flow rate. Radiation absorption by the catalyst was explicitly considered in the reaction rate expression. The degradation of a water pollutant, the pharmaceutical drug clofibric acid (CA), was evaluated in the microreactor under different flow rates, TiO_2 film thicknesses, and UV irradiation fluxes. The intrinsic kinetic parameter of CA degradation was extracted from the output data of the microfluidic reactor. The model was verified against numerical calculations of the full problem (advection, diffusion and reaction). Then, as an ultimate proof of the method, the obtained value of the kinetic parameter was successfully employed to predict the performance of a conventional, laboratory scale photoreactor. The proposed method constitutes a practical tool for laboratories dedicated to modeling, design and optimization of photocatalytic reactors for environmental applications. Apart from determining intrinsic parameters, the method also enables easy and quick catalyst screening.

1. Introduction

Photocatalysis with titanium dioxide represents a clean technology that involves many applications, including green synthesis of organic compounds, hydrogen production and environmental remediation. Particularly, photocatalysis applied to water purification constitutes an effective alternative technology to degrade chemicals that are resistant to conventional treatment methods: a wide range of non-biodegradable pollutants can be degraded under mild reaction conditions, employing near UV lamps or solar irradiation [1].

The presence of pharmaceuticals and personal care products in rivers, ground waters, and even in drinking water has increased public concern because of their potential adverse effects on human health and aquatic life. Specifically, clofibric acid (CA), the active metabolite of the lipid regulators clofibrate, etofibrate, and etofyllinclofibrate, has a very high persistence in the environment, with a half-life of 21 years. Indeed, it is one of the most frequently reported drug metabolites in open waters [2–4]. Photocatalysis with titanium dioxide (TiO_2) has been previously reported to effectively degrade CA in aqueous solutions; the

reaction intermediates and the possible reaction pathways have also been studied [5–7].

In order to design efficient devices to implement photocatalytic reactions, intrinsic kinetic parameters are needed. Furthermore, intrinsic kinetic information is required for objective comparison among different photocatalytic devices, as well as for catalyst screening, but reliable parameters are difficult to obtain in conventional reactors. Carefully planned experiments must be carried out, along with the derivation of complex models, to take into account the influence of radiation, mass transfer and fluid dynamics on the reaction rate. Alternatively, microreactors provide an excellent platform for photocatalytic kinetic studies based on the advantages of the microscale: laminar flow, short molecular diffusion distances, uniform irradiation, large surface to volume ratio, and accurate control of operation variables [8,9]. Additionally, small amounts of catalysts and reagents are needed, waste generation is minimal, and reliable results can be obtained employing short test times.

Different microreactors designs have been explored to carry out photocatalytic reactions [1]. Specifically, microfluidic reactors

---

configurations employed for water purification include micro-capillary reactors [10–12], single straight microchannel reactors [13–15], branched [16,17] and serpentine [8,18–20] multi-microchannel reactors, and planar microreactors [21,22]. A recent review summarizes fabrication techniques and substrates employed in microreactors for environmental applications [23].

Radiation modeling is one of the most relevant aspects to take into account when evaluating intrinsic kinetics. Even when mass transfer limitations can be avoided, the measured kinetics always depends on the radiation effectively absorbed by the catalyst. Therefore, to obtain intrinsic constants, reaction rate expressions must include a radiation absorption term [24]. This term depends mainly on the type of catalytic film, the amount of catalyst and the incident radiation flux. Different approaches to obtain intrinsic kinetic parameters in microreactors have been reported in the literature. Gorges et al. [16] presented a multiple microchannel reactor to obtain kinetic parameters of the photocatalytic degradation of the model pollutant 4-chlorophenol. By calculating Damköhler numbers, they demonstrated that mass transfer limitations could be neglected in their system. However, radiation absorption was not accounted for. Charles et al. [14] employed single microchannel reactors to evaluate kinetic constants of a photocatalytic reaction, the degradation of salicylic acid, but external mass transfer limitations and axial dispersion could not be avoided. As a result, the corresponding mass transfer coefficient and the axial dispersion coefficient had to be included in the modeling. Additionally, as the effect of radiation was not considered in the model, the obtained reaction rate constant depends on the light intensity absorbed by the catalyst. Visan and co-workers [8] presented a model to obtain kinetic parameters in microchannel reactors, where internal and external mass transport are accounted for. A light dependent model, based on a photon absorption carrier generation mechanism, was developed but, besides increasing the difficulty of the mathematical resolution, it involves a great number of unknowns. Therefore, a criterion for neglecting light intensity distribution in the catalyst layer was presented. In a follow-up paper [25], the light independent model was employed to extract kinetics of a photocatalytic reaction (degradation of methylene blue). Padoin et al. [26] employed the models proposed by Visan et al. [8] to compare the performance of TiO_2 and TiO_2-graphene catalysts for the degradation of methylene blue in a microchannel reactor. Radiation distribution was considered but a single value for the intrinsic kinetic constant could not be extracted and only apparent kinetic constants were reported. Krivec at al. [19] studied the kinetics of the photocatalytic oxidation of phenol in a fixed TiO_2 microreactor, under conditions of negligible internal and external mass transfer, but the dependence of the reaction rate on the radiation conditions could not be evaluated.

In this work, a simple analytical method for obtaining intrinsic kinetic constants for first order reactions in a photocatalytic microreactor is developed. A planar microreactor, with TiO_2 immobilized at the window, was specially designed and operated to avoid mass transfer limitations. The degradation of the pharmaceutical drug clofibric acid was evaluated under different flow rates, catalyst film thicknesses and UV illumination conditions. The influence of the TiO_2 film thickness and incident radiation was carried out through calculations of the radiation effectively absorbed by the catalyst. To verify the assumptions of the model, analytical results were compared against numerical calculations of the full problem (advection, diffusion and reaction). The first order kinetic parameter obtained with the analytical model in the microfluidic reactor was finally employed to predict the performance of a conventional, laboratory scale photoreactor. By comparison of experimental data and modeling results, the analytical proposal can be validated.

2. Experimental

2.1. Chemicals and analyses

Aeroxide® TiO_2 P25 from Evonik® was employed for the preparation of photocatalytic films over glass slides. Clofibric acid (CA) ($\geq 99.0\%$, $ClC_6H_4OC(CH3)_2CO_2H$) was purchased from Sigma Aldrich. CA concentration was measured, in triplicate, by HPLC with a UV detector using a Waters chromatograph provided with a RP C-18 column (YMC-Triart C18). The mobile phase was a binary mixture of acidified water (with 0.1% v/v phosphoric acid) and acetonitrile (50:50). Absorbance detection was made at 227 nm.

2.2. Preparation of the photocatalytic films

Borosilicate glass slides (6.5 cm × 2.5 cm × 0.3 cm) were first cleaned with a solution containing 20 g of potassium hydroxide, 250 mL of isopropyl alcohol, and 250 mL of ultrapure water. The slides remained in contact with the cleaning solution for 24 h. Then, they were calcined at 500 °C for 8 h to remove all possible traces of organic matter. The catalyst was immobilized over the glass slides by using a dip-coating process, following a technique adapted from van Grieken et al. [27]. A defined amount of TiO_2 powder was dispersed in ultrapure water at pH 1.5, adjusted with HNO_3. Each slide was dipped into the TiO_2 suspension at room temperature and extracted at a withdrawal speed of 3 cm/min. Subsequently, one side of the slide was wiped out with a soft tissue to obtain one-side coated glasses. Next, the slides were dried at 110 °C for 24 h and then calcined at 500 °C for 2 h using a heating rate of 5 °C/min. Suspensions of different TiO_2 concentrations were prepared to obtain three different film thicknesses. For the thinnest films, a suspension of 50 g/L of TiO_2 was employed (sample T1-50). To obtain an intermediate thickness, a suspension of 150 g/L of TiO_2 was used (sample T1-150). For the thickest films, two coatings employing the 150 g/L suspension were carried out, with the drying and calcinations steps in between (sample T2-150).

2.3. Catalyst film characterization

The amount of TiO_2 immobilized on the glass slides was measured by a spectrophotometric procedure adapted from Jackson et al. [28]. This technique involves the acidic digestion of the catalyst fixed on the glass support followed by the addition of H_2O_2 to produce a colored complex that is photometrically detected at 410 nm. The thicknesses of the catalytic films were calculated from cross-sectional SEM images of the coated glass slides, acquired by a scanning electron microscope (JEOL, JSM-35C) equipped with an acquisition system of digital images (SemAfore). Diffuse transmittance and reflectance measurements of the coated and bare glass slides were carried out with a spectrophotometer Optronic OL series 750, equipped with a reflectance integrating sphere (OL 740-70). A detailed description of the methodology employed can be found in Zacarías et al. [29].

2.4. Microreactor description

The microreactor consists of two main parts: (i) The housing for the glass slide, made of aluminum painted in black, with a rectangular window and an engraved space to fit the glass slide. (ii) The housing for the reaction cell, made of white Teflon, with round connectors for fluid inlet and outlet, and a micromachined planar reaction space (Fig. 1).

The dimensions of the reaction cell are 5.8 cm *long* × 2.0 cm *width* × 180 μm *height* (reactor volume V_R = 209 μL). The height of the reaction cell was measured with an Electronic Disk Micrometer (Schwyz™, China). The circular inlet/outlet ports have diffusers along the cell width, thus the fluid enters the reaction cell through the whole cross-sectional width and the flow becomes fully developed immediately after the inlet port (symmetric at the outlet).
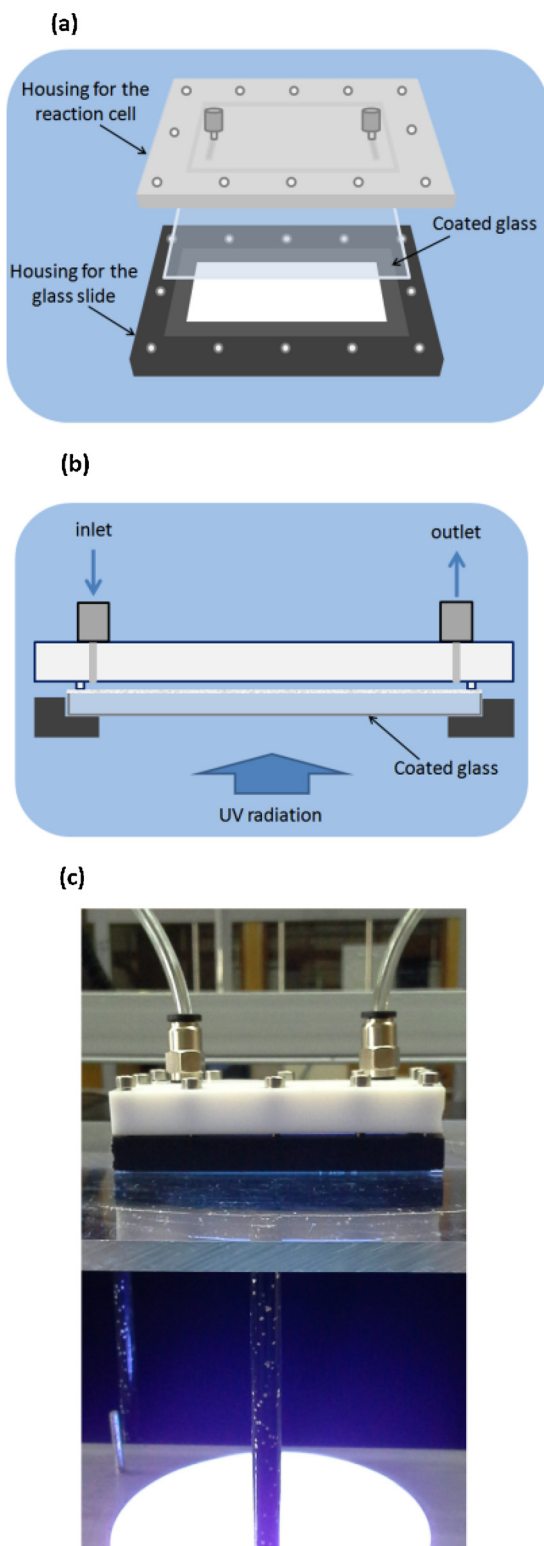
Fig. 1. (**a**) Scheme of the microreactor main components, (**b**) Reactor cross-section, (**c**) Photograph of the assembled reactor.

For operation, parts (i) and (ii) were assembled with the walls of the reaction cell (Teflon part) directly fitted on the glass surface. The sealing was assured by tightly adjusting 12 stainless steel Allen screws (Fig. 1c). This particular design allows easy assembly and disassembly of the reactor, and easy cleaning of all the reactor components. It represents a relevant feature because one can employ the same device with different catalytic films by only changing the glass slide.

2.5. Microreactor operation

Experiments were carried out by varying the following experimental conditions: the thickness of the TiO_2 films, h_0 (from 0.30 to 0.94 μm); the flow rate Q (from 15 to 330 μL/min); and the incident radiation level (two intensity levels). All experiments were performed in duplicate for each experimental condition, at the same initial concentration of CA and at the same initial pH: 20 mg/L of CA at pH 5 (natural pH of the solution of CA in distilled water), respectively.

Illumination was provided by 4 UV lamps (Philips TL 8 W Actinic BL), with maximum emission at 365 nm. The microreactor was placed at 11.5 cm from the lamps. In order to modify the irradiation level, an optical neutral filter was used to transmit ca. 30% of the total radiation. This filter, located between the lamps and the reactor, attenuates the incident radiation without altering the spectral distribution of the lamps. The resulting radiation fluxes at the reactor window were measured with a miniature spectrometer with optical fiber (USB 2000 + UV–vis-ES Ocean Optics). The sensor was located above a bare glass slide to account for the attenuation of the borosilicate glass. The measured fluxes between 340 and 400 nm, with and without the optical filter, were $0.26 \, mW/cm^2$ and $0.83 \, mW/cm^2$, respectively. The sensor was located at different positions throughout the window area, and the measured fluxes differed in less than 1%. Therefore, irradiation can be considered to be uniform at the reactor window. The spectral distribution of the irradiance at the reactor window is depicted in Fig. 2.

The aqueous solution of CA was injected into the reactor by a syringe pump (APEMA PC11UBT). Before the experiments, the emission of the lamps was stabilized and the adsorption equilibrium between the pollutant and catalyst was reached. For each assay, the outlet solution was collected in a glass vial before HPLC analysis. Control experiments were carried out in the reactor with a bare glass slide to evaluate the direct photolysis of the pollutant. No detectable changes in the concentration of CA were found in the absence of catalyst.

2.6. Conventional photoreactor description and operation conditions

Experimental data previously obtained in a conventional reactor, and reported in ref [24], was employed to validate the proposed methodology. This laboratory scale device consists of a cylindrical glass reactor (5 cm diameter × 2.75 cm length) with two circular flat windows, a tank, and a centrifugal pump. It operated as a fixed-film, perfectly mixed, batch reactor with recycle. The reactor volume was 54 mL, and the total volume of the reacting solution in the system was $V_T = 1000 \, mL$. It was illuminated through one of the windows by a halogenated mercury lamp (150 W Powerstar HQI-TS from OSRAM). The incident radiation flux at the reactor window, between
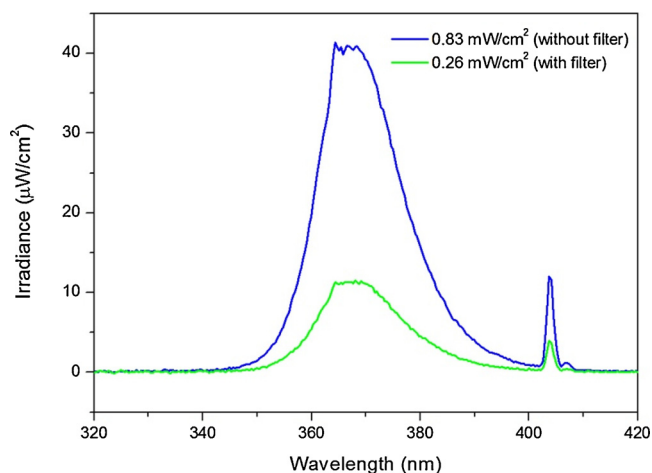

Fig. 2. Spectral irradiance at the reactor window.

350–410 nm, was $5\,mW/cm^2$. To carry out experiments with a lower irradiation level, an optical neutral filter was placed between the reactor and the lamp, attaining an incident flux of $3\,mW/cm^2$. The catalyst (TiO_2 Aeroxide P25) was immobilized over the inner face of the illuminated reactor window by the dip-coating procedure (area coated by the catalyst: $19.6\,cm^2$). Three different catalytic film thicknesses were evaluated: 0.65, 1.70, and $2.70\,\mu m$. Internal and external mass transfer could be safely neglected in the system.

To carry out the degradation experiments, solutions of $20\,mg/L$ of CA, at natural pH, were added to the tank and circulated in the reactor for 60 min to achieve the adsorption equilibrium between CA and the TiO_2 film. During this time, the solution was saturated with pure oxygen by intense bubbling and the lamp was turned on to stabilize the radiation emission. To prevent the arrival of radiation at the reactor, a shutter was placed between the lamp and the reactor window. When the system was stabilized and the adsorption equilibrium was reached, the first sample was taken from the tank and then the shutter was removed. Throughout the reaction, the system was maintained under overpressure of oxygen to guarantee the renewal of the oxygen consumed. Each experiment lasted 480 min, and samples were taken every 60 min.

3. Modeling

3.1. Mass transport and reaction model in the microreactor

The reaction cell was designed to attain uniform fields of both fluid velocity and radiation throughout the flow domain, as well as negligible diffusion limitations in the fluid and solid (porous) phases. If these requisites are satisfied, intrinsic kinetic constants can be obtained from experimental data by a simple linear analysis, as described below.

3.1.1. Reaction mechanism

The following mechanism has been proposed in the literature for the photocatalytic degradation of clofibric acid with titanium dioxide [5–7]: the absorption of UV radiation by the catalyst promotes electrons from the valence band of the semiconductor into the conduction band, leaving positively charged holes in the valence band. The photogenerated holes can migrate to the surface of the catalyst particle and react with water molecules or hydroxyl ions adsorbed at the catalyst surface, leading to the formation of hydroxyl radicals. In turn, hydroxyl radicals can attack CA molecules to give two primary organic intermediates: 4-chlorophenol (4-CP) and benzoquinone (BQ). Also, 4-CP can be further degraded by oxidation with hydroxyl radicals, giving BQ and other secondary organic intermediates.

3.1.2. Reaction rate

In photocatalytic reactions, the dependence of the reaction rate on the absorbed radiation can take two limiting values [30–32]. For high values of absorbed radiation by the catalyst, the reaction rate is proportional to the square root of the photon absorption rate. On the contrary, when the absorbed radiation is low, the dependence of the reaction rate on the photon absorption rate results linear.

Based on our previous experiments under similar operating conditions, the rate of disappearance of CA was assumed to be of first order with respect to the concentration of CA, and square root order with respect to the absorbed radiation by the catalyst [24]. Therefore, assuming uniform irradiation of the TiO_2 film, and negligible mass transfer limitations, the volumetric rate of CA photocatalytic degradation r [$mol/(s\,cm^3)$] in the reaction cell can be expressed as

$$r = -k\frac{A_{cat}}{V_R}(\langle e_f^{a,s}\rangle_{A_{cat}})^{0.5}C \tag{1}$$

where k represents the intrinsic kinetic constant involved in the photocatalytic degradation of CA [$cm^2/(s^{0.5}\,einstein^{0.5})$], A_{cat} is the irradiated area of TiO_2-coated surface [cm^2], V_R is the reaction cell volume
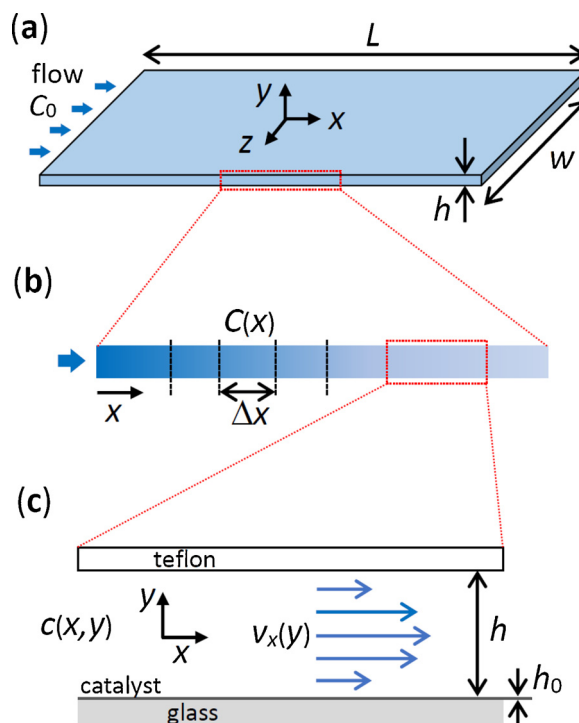

Fig. 3. Schematic representations of (**a**) the flow domain geometry (out of scale) and coordinate system, (**b**) a simplified unidirectional view of the reaction zone with average reagent concentration in the gap, and (**c**) details of the flow field in the reaction cell.

[cm^3], C is the bulk concentration of CA [mol/cm^3], and $\langle e_f^{a,s}\rangle_{A_{cat}}$ is the local surface rate of photon absorption (SRPA) [$einstein/(s\,cm^2)$] averaged over A_{cat}; that is, the amount of photons absorbed per unit time and per unit area of irradiated TiO_2-coated surface. By defining the term $\frac{A_{cat}}{V_R}(\langle e_f^{a,s}\rangle_{A_{cat}})^{0.5}$ as the radiation factor F_{rad}, and the apparent first order kinetic constant as

$$k_{app} = kF_{rad} \tag{2}$$

the reaction rate expression results $r = -k_{app}C$.

3.1.3. Microreactor design and operating conditions

Two main features were addressed in designing the reaction cell geometry: large aspect ratios, which were set $L/h > 300$ in the flow direction and $w/h > 100$ in the transverse direction, and small gap thickness, which was chosen thin enough ($h = 180\,\mu m$) to attain diffusion times shorter than reaction times. The cell geometry is sketched in Fig. 3a, where the entrance and exit regions are omitted, since these zones are not irradiated, and the flow area with non-uniform streamlines is negligibly small. For steady state and very low Reynolds numbers ($Re < 0.2$ in our experiments), the flow field is equivalent to that attained between two infinitely large parallel plates (Hele-Shaw flow). As illustrated in Fig. 3c, the fluid velocity is established in the x-direction and varies in the y-direction only.

During operation, the reagent molecules are advected by the flow on streamlines parallel to the reaction plate (catalyst film); then molecules diffuse transverse to the flow to reach the reaction sites on the lower plate. The relative importance of these processes is evaluated from the respective time scales. The advective transport is characterized by the residence time: $t_R = V_R/Q$, where $V_R = Lwh$ is the reaction volume and Q is the flow rate. For $V_R = 209\,\mu L$ and the flow rates used in practice, 15–330 $\mu L/min$, the residence times were 836-38 s, respectively. The diffusion time is quantified as the time required by the molecular transport process to span reactants in the reactor gap: $t_D = h^2/D$, where D is the molecular diffusion coefficient. For $D \approx 1.0 \times 10^{-9}\,m^2/s$ [33],

Table 1
Characteristic times and related dimensionless numbers.

Name	Symbol	Definition	Values (Q = 15–330 μL/min)
Residence time	t_R	V_R/Q	840–40 s
Diffusion time (in the fluid)	t_D	h^2/D	30 s
Effective diffusion time (in the porous solid phase)	t_{D_e}	h_0^2/D_e	0.007 s
Reaction time	t_k	$1/k_{app}$	60 s
Péclet number	Pe	t_D/t_R	0.04–0.8
Damköhler I number	Da_I	t_R/t_k	14–0.7
Damköhler II number	Da_{II}	t_D/t_k	0.5
Thiele modulus	ϕ	$(t_{D_e}/t_k)^{0.5}$	0.01

the diffusion time is around 30 s. To quantify diffusion inside the porous solid phase (TiO_2 film), the effective diffusion time $t_{D_e} = h_0^2/D_e$ is employed, where $D_e = D\varepsilon/\tau$ represents the effective diffusion coefficient, ε is the porosity, and τ is the tortuosity of the film. Considering $\varepsilon = 0.45$ and $\tau = 3.0$ [34], $t_{D_e} \approx 0.007$ s for the thickest film. Finally, the characteristic reaction time can be estimated as the reciprocal of the kinetic rate constant: $t_k = 1/k_{app}$. From preliminary studies, the value of k_{app} was estimated under the conditions of highest reaction rate (highest irradiation and thickest catalyst film). The resulting t_k is 60 s, which represents the fastest reaction kinetics in this work. These characteristic times are summarized in Table 1 for further scaling analysis.

The operating conditions of the microreactor were defined in the theoretical framework of microprocess engineering [35]. A scaling analysis from the relevant dimensionless numbers was carried out. As outlined in Table 1, Péclet (*Pe*, diffusion to flow times ratio), Damköhler I (*Da_I*, flow to kinetic times ratio), and Damköhler II (*Da_II*, diffusion to kinetic times ratio) numbers, and the Thiele modulus (ϕ, internal diffusion to kinetic times ratio) are used to fully characterize the photoreactor. According to the rigorous study of Aillet et al. [36], when both *Pe* and *Da_II* are lower than 1, the microreactor operates in the zone where the concentration is rather homogeneous in the *y*-direction at the cell outlet. This is precisely the operating zone reached in our system, according to the characteristic times estimated above: molecular diffusion is faster than both the chemical reaction and the advective transport (even at the highest flow rates used); hence the photoreaction occurs in the reaction-limited condition.

In order to better illustrate the physical meaning of the scaling analysis, Fig. 4 presents a diagram build from the relevant dimensionless numbers listed in Table 1 (see also ref. [36]). In addition, here we include the operating zone of our system in comparison to those of typical microfluidic photoreactors [14,25]. Other reported systems lay out of the diagram boundaries, as they were operated at either extremely large [8] or extremely small [16] *Da_II* numbers. Further discussions on this issue are given below in Section 4.5.

Additional arguments supporting the geometrical design are found in the analysis reported by Squires et al. [37], where the ratio between the length of the reaction plate and the cell gap was considered to be a critical parameter to define the operating conditions (see also Gervais and Jensen [38]). Since this ratio is $L/h = 320$ for the microreactor designed in this work, and considering that $Pe < 1$, the reactant concentration preponderantly changes along the flow path, as sketched in Fig. 3b (see also the numerical prediction for small *Pe* numbers on Fig. 8), which is equivalent to assume that diffusive limitations are negligible for the photoreaction. Besides, the large width/height ratio of the flow cell ensures that concentration is uniform along the *z*-direction.

The influence of mass transfer inside the porous TiO_2 film was estimated by the Thiele modulus [24,39]. A value of $\phi < < 1$ indicates that internal mass transfer resistance is negligible. The value computed for ϕ under the most unfavorable situation (thickest film and highest
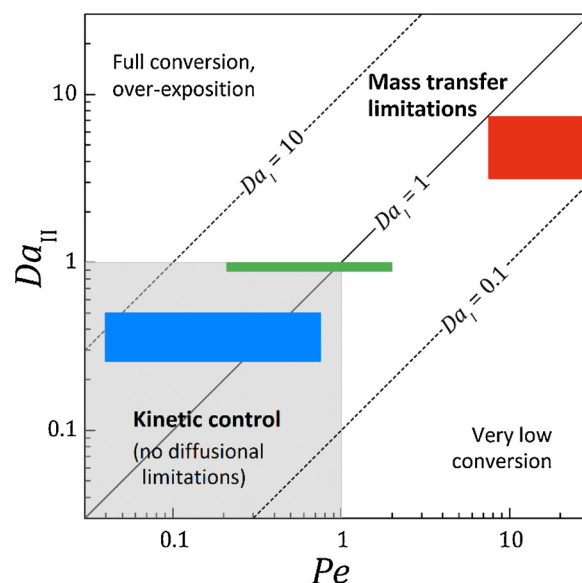

Fig. 4. Damköhler II-Peclet diagram showing the relative predominance of each mass transport phenomenon in the reaction cell. The Damköhler I lines indicate the zones of high (top-left) and low (bottom-right) conversion. The light gray region denotes the conditions required to operate under kinetic control, i.e. with minimized mass transfer limitations. The colored rectangles represent the operation range of different photocatalytic microreactors: red, Ref. [14]; green; Ref. [25]; blue, present work (For interpretation of the references to colour in this figure legend, the reader is referred to the web version of this article).

irradiation) is 0.01. Therefore, the reaction rate can be safely assumed to occur in the catalytic film without internal mass transfer limitations.

3.1.4. Analytical model of the reaction cell

Comprehensive theoretical models for surface reactions in microreactors are available [37,38,40,41], which involve the coupling of convective transport, molecular diffusion, and chemical reactions. In addition, rigorous modeling of photocatalytic microreactors considers the mass transfer in the catalyst porous layer, as well as the photon flux density for the radiation dependent conversion [8,34,36]. Implementing these formulations invariably requires numerical computations, which makes the identification of critical parameters rather impractical. In contrast, here we derive a simple mathematical model that accounts for the dominant mass transfer mechanisms in the reaction cell, and explicitly includes the key system parameters. Furthermore, the model allows one to assess the intrinsic kinetic constant from experimental data measured in the microreactor. This strategy is possible because the microreactor was designed to work in the operating zone where all the merits of microfluidic devices can be exploited, notably the minimization of diffusional limitations (light gray zone in Fig. 4), as explained above.

In fact, given that molecular transport is highly efficient in the cell gap, the reactant concentration changes principally along the flow direction, and the 2D concentration field can be reduced to a 1D field, with the average concentration *C* varying in the *x*-direction only. Further, the unidirectional flow in *x*-direction can be divided into differential intervals Δx, as illustrated in Fig. 3b. Under these conditions, a balance of the reagent moles in any elementary reaction volume $V_{\Delta x} = wh\Delta x$ is expressed [35],

$$QC|_{in} - QC|_{out} = rV_{\Delta x} \tag{3}$$

where *QC* are the moles of reagent (per unit time) entering/leaving the elementary reaction volume with the flow and $rV_{\Delta x}$ is the conversion rate, *r* being the reaction rate. Taking into account the fluid mass conservation, Eq. (3) can be rewritten as $\Delta C/\Delta x = rwh/Q$. Calculating the limit of $\Delta C/\Delta x$ for $\Delta x \to 0$ leads to the following differential

equation,

$$\frac{dC}{dx} = -\frac{wh}{Q}r(C)$$ (4)

The reaction rate can be included in the general form $r(C) = -k_{app}C^m$, where $m = 0$, 1, and 2 stands for zero, first, and second order kinetics, respectively. Another reaction rate equation frequently used in photocatalysis is the Langmuir-Hinshelwood model, $r(C) = -k_{app}KC/(1 + KC)$, where K is an equilibrium adsorption constant [14–16].

In what follows we employ the first order kinetics, $r(C) = -k_{app}C$, which is appropriate for CA, as described above in Eq. (1). Integrating Eq. (4) with the initial condition $C(x = 0) = C_0$ (reactant concentration at the reactor inlet) yields,

$$\frac{C(x)}{C_0} = \exp\left(-\frac{k_{app}wh}{Q}x\right)$$ (5)

which describes the variation of the average reagent concentration along the reaction cell. In addition, by defining $C(x = L) = C_L$ as the average concentration at the outlet, one may describe the reaction conversion as follows,

$$\frac{C_0 - C_L}{C_0} = 1 - \exp\left(-\frac{k_{app}V_R}{Q}\right) = 1 - \exp(-Da_I)$$ (6)

This relationship quantitatively predicts the microreactor conversion as a function of the operating flow rate, for a given reaction rate. The second equality in Eq. (6) makes evident the role played by the Da_I number: the conversion is controlled by the interplay between the residence and reaction times [36]. For example, if the flow is relatively fast, or the reaction is very slow, a fraction of reactants could not reach the reaction sites before exiting the reactor (bottom-right zone in Fig. 4). Thus Eq. (6) successfully captures the influence of flow rate, which is critical to optimize the conversion efficiency.

The procedure suggested here to extract k_{app} is based on the following equation, which is obtained by reordering Eq. (6):

$$\frac{Q}{V_R} = k_{app}\left[\ln\frac{C_0}{C_L}\right]^{-1}$$ (7)

Therefore, a straightforward plot of Q/V_R vs $1/ln(C_0/C_L)$ allows one to obtain the apparent rate constant k_{app} from the curve slope. Experimental values of C_L and C_0 for different Q need to be obtained in a microreactor operating in the zone of $Pe < 1$ and $Da_{II} < 1$ (light gray zone in Fig. 4), where the characteristic diffusion time is shorter than both residence and kinetic times, as described in Section 3.1.3. If these conditions are satisfied, Eq. (7) is a practical tool to determine intrinsic kinetic constants in photoreactors, avoiding the use of demanding computational resources. Precisely, this simple model is verified here against numerical calculations of the full transport problem (advection, diffusion and reaction).

Concerning the reaction rate models, it should be added that similar plots can be exercised for zero (Q/V_R vs $C_L - C_0$) and second (Q/V_R vs $1/C_L - 1/C_0$) order reactions. In particular, the case of Langmuir-Hinshelwood kinetics has been treated in ref. [14].

3.1.5. Numerical model of the full problem

Numerical simulations were performed with OpenFOAM® version 4.1, a program based on the finite volume method. Particularly, pimpleFoam solver was used for solving the fluid flow and a modified version of the scalarTransportDecay solver was used for solving the transport-reaction equation. As OpenFOAM® natively provides 3D support, the calculation domain reproduces the reaction cell with all the corresponding dimensions (Fig. 3a). Therefore, mass transfer processes (including diffusion) were calculated for the actual configuration of the microreactor, where the photoreaction takes place at the lower plate (Fig. 3c). Simulations were carried out for the operating

conditions employed in experiments.

The fluid velocity field was solved by using the complete transient Navier-Stokes equation for incompressible Newtonian fluids:

$$\rho\left(\frac{d\mathbf{v}}{dt} + \mathbf{v}.\nabla\mathbf{v}\right) = -p\mathbf{I} + \mu(\nabla\mathbf{v} + \nabla\mathbf{v}^T)$$ (8)

$$\rho(\nabla.\mathbf{v}) = 0$$ (9)

where $\mathbf{v}$ is the fluid velocity, p the pressure, and $\mathbf{I}$ the identity tensor. Fluid density $\rho = 1000 \, kg/m^3$ and viscosity $\mu = 0.001 \, Pa$ were used in calculations. The boundary conditions were imposed as follows: uniform inlet velocity in the x-direction (according to the flow rate), zero pressure at the outlet, and zero fluid velocity at the reactor walls (no-slip condition). Once the velocity field was obtained, the concentration field was calculated by using the advection-diffusion equation, which includes the chemical reaction as a sink term:

$$\frac{dc}{dt} + \nabla.(\mathbf{v}c - D\nabla c) = -k_{app}c$$ (10)

In this expression, $c(x, y, z)$ represents the local reagent concentration at each point in the flow domain, while capital $C(x)$ defined in the previous section stands for the average concentration in the cell cross-section. The diffusion coefficient value used in simulations was $D = 1.0 \times 10^{-9} \, m^2/s$. The corresponding boundary conditions were imposed as follows: uniform concentration C_0 at the inlet and insulating condition at the walls. It is worth noting that, instead of including the reaction term as the boundary condition at the lower plate (catalyst layer), here the problem is formulated as a homogeneous system. In this format, the photoreaction must (numerically) operate on the close vicinity of the lower plate only, thus the kinetic constant k_{app} was implemented as follows:

$$k_{app} = \begin{cases} 0, & y > h_0 \\ k_{app}, & y \leq h_0 \end{cases}$$ (11)

where h_0 is the catalyst film thickness (Fig. 3c). To properly capture this process, the discretization mesh was refined near the bottom plate (grading in y-direction), with the minimum mesh size approaching the catalyst layer thickness: 0.25, 0.5 and 1 μm for samples T1-50, T1-150 and T2-150, respectively (see Table 2). Therefore, in the worst conditions, the zone $0 \leq y \leq h_0$ represented only 0.5% of the whole flow domain.

The numerical value of k_{app} was obtained as a fitting parameter by comparing numerical outputs against experimental results, for the same operating conditions. That comparison requires the numerical evaluation of the output concentration. For this purpose, the mixing-cup average concentration was obtained as follows,

$$C_L = \frac{\int cvdA}{\int vdA} = \frac{1}{Q}\iint c(L, y, z)v(L, y, z)dydz$$ (12)

3.2. Radiation model

For the purpose of obtaining the value of the intrinsic parameter k from k_{app}, radiation absorption in the catalytic film must be evaluated (Eq. (2)). This section describes the procedure to calculate the value of $\langle e_f^{a,s}\rangle_{A_{cat}}$ for different irradiation conditions and catalyst thicknesses in the microreactor. When a radiation beam traverses the TiO₂ film, its

Table 2
Main characteristics of the catalyst films.

Catalyst Sample	TiO₂ content (mg/cm²)	Film thickness (μm)	$\sum_\lambda \alpha_{f,\lambda} \varphi_\lambda$
T1-50	0.17 ± 0.03	0.30 ± 0.04	0.22
T1-150	0.31 ± 0.03	0.56 ± 0.04	0.40
T2-150	0.63 ± 0.04	0.94 ± 0.05	0.48

intensity changes due to three events: light absorption, reflection, and transmission. Therefore, by applying a local radiative energy balance in terms of the local net radiation fluxes, the local SRPA ($e_f^{a,s}$) on the photocatalytic film can be calculated as

$$e_f^{a,s} = q_{f,in} - q_{f,tr} - q_{f,rf} \qquad (13)$$

where $q_{f,in}$ is the local radiative flux that reaches the catalytic film, $q_{f,tr}$ the local radiative flux transmitted through the film, and $q_{f,rf}$ the local radiative flux reflected by the TiO$_2$ film. Because the catalytic film is assumed to be uniformly irradiated, the average SRPA over the irradiated area A_{cat} can be obtained by averaging the local fluxes:

$$\langle e_f^{a,s} \rangle_{A_{cat}} = \langle q_{f,in} \rangle_{A_{cat}} - \langle q_{f,tr} \rangle_{A_{cat}} - \langle q_{f,rf} \rangle_{A_{cat}} \qquad (14)$$

The average SRPA can also be expressed as a function of the incident radiation flux as

$$\langle e_f^{a,s} \rangle_{A_{cat}} = \langle q_{f,in} \rangle_{A_{cat}} \sum_\lambda \alpha_{f,\lambda}\, \varphi_\lambda \qquad (15)$$

where $\alpha_{f,\lambda}$ is the fraction of energy absorbed by the TiO$_2$ film at wavelength λ, φ_λ is the normalized fraction of the radiation that reaches the film at wavelength λ, and $\sum_\lambda \alpha_{f,\lambda}\, \varphi_\lambda$ is the summation of the product of both quantities over the wavelength range of interest.

The absorbed fraction of energy of a catalytic film $\alpha_{f,\lambda}$ can be computed as:

$$\alpha_{f,\lambda} = 1 - T_{f,\lambda} - R_{f,\lambda} \qquad (16)$$

where $T_{f,\lambda}$ and $R_{f,\lambda}$ represent the fraction of energy transmitted and reflected by the TiO$_2$ film at wavelength λ. $T_{f,\lambda}$ and $R_{f,\lambda}$ cannot be directly measured from a film without support, but they can be computed from the experimental values of diffuse transmittance (T) and reflectance (R) of TiO$_2$ coated and bare plates. The following expressions, obtained by applying the Net-Radiation method [42] to the photocatalytic glass slides, relate the values of transmittance and reflectance of the TiO$_2$ film (f), the bare glass slide (glass, g), and the coated glass slides (film + glass, fg):

$$T_{f,\lambda} = \frac{T_{fg,\lambda}}{T_{g,\lambda}}(1 - R_{f,\lambda} R_{g,\lambda}) \qquad (17)$$

$$R_{f,\lambda} = \frac{R_{fg,\lambda} T_{g,\lambda}^2 - T_{fg,\lambda}^2 R_{g,\lambda}}{T_{g,\lambda}^2 - T_{fg,\lambda}^2 R_{g,\lambda}^2} \qquad (18)$$

Diffuse transmittance and reflectance measurements were carried out for the three catalyst samples, between 340 and 400 nm. More information on the experimental procedure can be found in Section 2.3 and reference therein. For the two irradiation conditions, the values of $\langle q_{f,in} \rangle_{A_{cat}}$ were measured experimentally, as detailed in Section 2.5. Therefore, the values of $\langle e_f^{a,s} \rangle_{A_{cat}}$ were computed with Eq. (15) for each catalyst sample and for each incident radiation level.

4. Results and discussion

4.1. Film characterization

Fig. 5 shows scanning electron micrographs of sample T1-150, where a high degree of homogeneity on the surface and thickness of the film can be observed. Images of similar aspect were obtained with the other coated slide samples.

Table 2 presents results of the TiO$_2$ mass content, the thickness of the films and the polychromatic absorption term $\sum_\lambda \alpha_{f,\lambda}\, \varphi_\lambda$. from Eq. (15), for the three catalyst samples. The increase in TiO$_2$ content of the samples corresponds to the increase in the film thickness. The absorption term also increases with the mass of catalyst, but the effect is not linear.

4.2. Photocatalytic experiments and kinetic parameter estimation

The photocatalytic degradation pathway of clofibric acid with TiO$_2$, as discussed in Section 3.1.1, involves the formation of the primary intermediate 4-chlorophenol and benzoquinone [7]. However, in our microreactor experiments, only 4-chlorophenol was detected. In Fig. 6a, the conversion of clofibric acid in the microreactor is depicted as a function of the flow rate, for the two irradiation conditions, with the sample T1-150. In Fig. 6b, data from the same experiments are plotted as Q/V_R vs. $1/\ln(C_0/C_L)$, in order to calculate the apparent kinetic constants directly from the curve slopes.

As observed in Fig. 6a, complete degradation of clofibric acid was achieved at low flow rates (Q = 15 μL/min), employing T1-150 for both irradiation conditions. Conversion of CA decreases when the flow rate increases, as a result of the reduction in the residence time of the pollutant molecules inside the reactor. The effect of the irradiation level is evidenced at high flow rates, where a clear enhancement of the pollutant conversion is observed when irradiation raises from 0.26 to 0.83 mW/cm^2. As illustrated in Fig. 6b, data employing the same catalyst sample and irradiation level falls on a linear plot, thus validating the assumption of first order reaction with respect to the pollutant concentration, as well as the 1D transport model (additional verifications are given below). The same methodology was employed with the other catalyst samples. Results of the apparent kinetic constants (with the 95% confidence interval) for each catalyst sample, under the two irradiation levels, are presented in Table 3. The corresponding values of the incident radiation fluxes $\langle q_{f,in} \rangle_{A_{cat}}$ and the average surface rate of photon absorption $\langle e_f^{a,s} \rangle_{A_{cat}}$ are included in the table.

The square root dependence of the reaction rate on the absorbed radiation can be verified by plotting the values of k_{app} vs F_{rad} (Eq. (2)), as reported in Fig. 7a. From the slope of this plot, the value of the intrinsic constant k is calculated. The analytical model rendered k= 10.0 (± 0.9) cm^2/(s$^{0.5}$ einstein$^{0.5}$). The values of k_{app} obtained from numerical calculations of the full problem were also plotted vs F_{rad}, giving k= 11.2 (± 0.9) cm^2/(s$^{0.5}$ einstein$^{0.5}$). As both methods provide similar values of the kinetic constant, and their respective confidence intervals are overlapped, the assumptions made in the derivation of the analytical model (Eq. (7)) can be considered valid. It is worth to remark that this calculation method actually requires a photocatalytic microreactor with minimized diffusional effects, such as the one designed and used in this work.

Furthermore, the single value of k is able to represent the conversion of CA for all the flow rates, catalyst samples, and irradiation conditions in the microreactor. Fig. 7b compares the conversion calculated with the estimated kinetic parameter against experimental data. A remarkable agreement can be observed for all the catalytic samples and flow rates.

4.3. Numerical simulations

Fig. 8 presents numerical results of the CA concentration field in the reaction cell, made dimensionless with C_0, under different flow rates. Calculations were carried out by using the complete transport model, as described in Section 3.1.5. It is worth noting that the aspect ratio of the actual reaction cell is L/h = 320, which makes impossible to graphically illustrate the concentration field in the whole flow domain. Thus, for the sake of clarity in the analysis, the aspect ratio has been deliberately decreased to approximately 6 in Fig. 8. It can be seen that, at low flow rates (Fig. 8a and b), all the reactant is converted in the first portion of the cell and 100 % conversion is reached at the outlet. This limit of very low Pe numbers is the ideal regime to satisfy the hypothesis made in modeling (Fig. 3b): the concentration varies predominantly in the x-direction. Nevertheless, most of the reaction cell is unexploited in this regime, as the degradation is fulfilled in the first portion of the flow domain. On the other hand, at the largest flow rates (Fig. 8d), around 50% conversion is obtained at the cell outlet. In this case, a
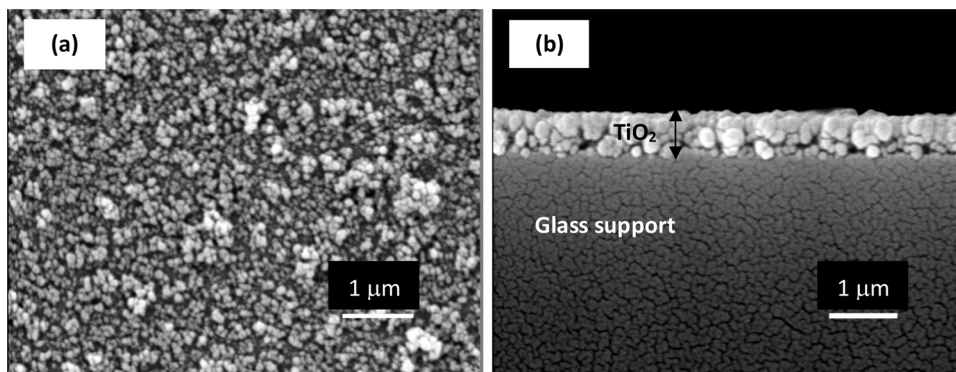
Fig. 5. SEM images of the TiO$_2$ films (sample T1-150). (**a**) Top view. (**b**) Cross section.
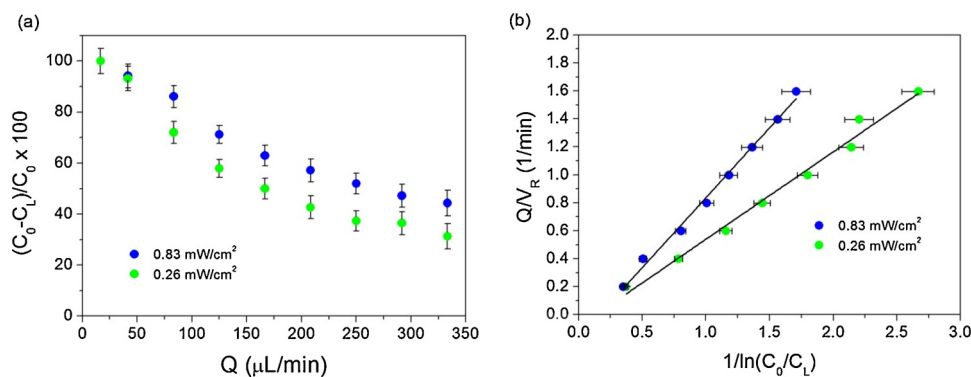

Fig. 6. Degradation of clofibric acid with sample T1-150, under different irradiation conditions. (**a**) Conversion vs. flow rate. (**b**) Plot of Eq. (7) to extract k_{app} from the curve slopes (see Table 3).

Table 3
Apparent kinetic constants for different catalyst samples and irradiation conditions.

Catalyst Sample	$\langle q_{f,in}\rangle_{A_{cat}}$		$\langle e_f^{a,s}\rangle_{A_{cat}}$	k_{app} [1/min]
	[mW/cm^2]	[einstein/(s cm^2)]	[einstein/(s cm^2)]	
T1-50	0.26	8.0×10^{-10}	1.7×10^{-10}	0.47 ± 0.04
T1-50	0.83	2.5×10^{-9}	5.5×10^{-10}	0.90 ± 0.10
T1-150	0.26	8.0×10^{-10}	3.2×10^{-10}	0.63 ± 0.07
T1-150	0.83	2.5×10^{-9}	1.0×10^{-9}	0.99 ± 0.08
T2-150	0.26	8.0×10^{-10}	3.8×10^{-10}	0.80 ± 0.07
T2-150	0.83	2.5×10^{-9}	1.2×10^{-9}	1.10 ± 0.10

concentration gradient is formed in the y-direction, hence the reactant molecules diffuse to the catalytic film, but the residence time is not enough to allow the conversion of all the reactant molecules. At intermediates flow rates (Fig. 8d), the longer residence times allow higher conversions, which reach approximately 70% at the cell outlet.

These numerical results also show that the one-dimensional modeling carried out in Section 3.1.4 (depicted in Fig. 3b) is reasonably well justified, taking into account that the actual aspect ratio of the cell is 320. Evidently, for the largest flow rates (increasing Pe numbers), a concentration gradient necessarily develops in the transverse y-direction, but reactant molecules still diffuse faster than the degradation rate ($Da_{II} < 1$), and mass transfer limitations are negligible. Furthermore, as mentioned above, these figures correspond to $k = 11.2 \ (\pm 0.9)$ cm^2/(s$^{0.5}$ einstein$^{0.5}$), meaning that the numerically predicted concentration at the cell outlet (right end of Fig. 8a–d) coincides to the prediction of
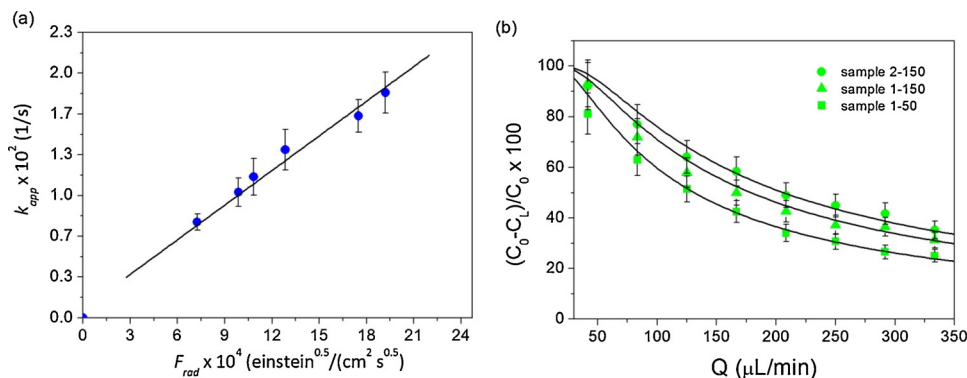

Fig. 7. (**a**) Apparent kinetic constant vs radiation factor F_{rad}. Symbols are experimental data and the full line is Eq. (2), where the slope $k = 10.0 \ (\pm 0.9)$ cm^2/(s$^{0.5}$ einstein$^{0.5}$) is obtained as a fitting parameter. (**b**) Degradation of CA at different flow rates for the three catalyst samples subjected to an incident radiation flux of 0.26 mW/cm^2. Symbols are experimental data and the solid lines are the model predictions (Eq. (6)) with $k = 10.0 \ (\pm 0.9)$ cm^2/(s$^{0.5}$ einstein$^{0.5}$) in all cases.
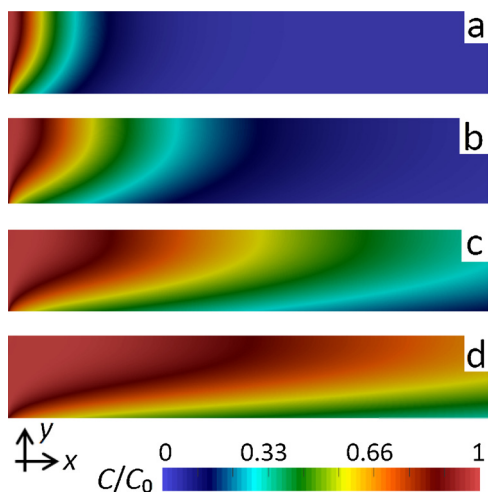
Fig. 8. Numerical simulations of the concentration field inside the reaction cell for different flow rates Q: (**a**) 17; (**b**) 42; (**c**) 128; (**d**) 300 µL/min. Sample T1-150. Incident radiation flux: 0.83 mW/cm^2. The contour plots are deliberately out of scale for better visualization (the actual y-x aspect ratio of the reaction cell is 320).

the analytical model, and hence to experimental values.

4.4. Validation of the proposed method

In order to validate the analytical method, the resulting intrinsic kinetic constant [k=10.0 (± 0.9) cm^2/(s$^{0.5}$ einstein$^{0.5}$)] was employed to predict the performance of a conventional, laboratory scale reactor (See Section 2.6).

The expression for the mass balance of CA in the laboratory reactor is,

$$\frac{dC}{dt} = -k\frac{A_{cat}}{V_T}(\langle e_f^{a,s}\rangle_{A_{cat}})^{0.5}C \tag{19}$$

with the corresponding initial condition $C(t = 0) = C_0$ [24].

Fig. 9 presents experimental data and model predictions of the concentration of clofibric acid vs irradiation time in the lab scale reactor, under different irradiation fluxes and film thicknesses.

It is important to highlight that no adjustable parameters were employed in the calculations with Eq. (19). The intrinsic kinetic parameter was directly introduced into the mass balance of CA in the laboratory reactor, and the values of $\langle e_f^{a,s}\rangle_{A_{cat}}$ were calculated following the procedure described in Section 3.2. These results demonstrate that the (previously calculated) kinetic constant can adequately predict the evolution of the concentration of CA in a conventional reactor, under different conditions of irradiation and film thicknesses, thus proving its intrinsic character. It should be remarked that this kinetic constant is valid under conditions of high radiation absorption (square root

dependence of the reaction rate on the photon absorption rate). In fact, as it was demonstrated in this work, an incident radiation flux of 0.26 mW/cm^2 and a TiO$_2$ film thickness of 300 nm can already assure this condition. Taking into account that most reported experiments on photocatalytic reactions employ irradiation levels above 1 mW/cm^2, the kinetic constant is widely applicable.

4.5. Overall discussions

It is worth to stress that the photocatalytic microreactor has been specially designed to operate under conditions of negligible diffusional limitations, where the relevant characteristics are the Hele-Shaw flow domain, the catalyst film thicknesses, and the UV illumination conditions. Concerning the fluid dynamics and mass transfer, one may observe in Fig. 4 the advantages of our experimental design in comparison with similar systems previously reported. Of course, one can adjust the system parameters to operate in a more ideal situation of kinetic control (bottom-right corner in Fig. 4), which can be simply done by decreasing the cell height h, as it strongly lowers the diffusion time ($t_D = h^2/D$). This is the case of photo-reactors with small microchannels, such as the one reported in Ref. [16] (see also Ref. [1]), which operates at $Pe < 1$ and extremely low Da_{II} numbers (out of the plot range of Fig. 8). However, these configurations involve low throughputs because of the high pressures required to drive fluids in the resulting resistive circuit. To circumvent this problem, the system reported here satisfies a tradeoff between controlling diffusional effects and attaining reasonable throughputs.

The used model has been formulated for the ideal conditions of kinetic control, which presuppose that the reagent concentration gradient changes predominantly along the flow direction. Numerical simulations show that this hypothesis is well justified at low Pe numbers (Fig. 8a and b). At higher Pe numbers, the reagent concentration varies in the transverse direction as well (Fig. 8c and d), but the model is still applicable, provided that the degradation rate is smaller than the diffusion rate, i.e. as long as $Da_{II} < 1$. Hence, the intrinsic kinetics can be extracted by using analytical formulae, without computing the mass transfer effects. In contrast, the model should not be employed, unless in its present form, for systems operating out of the light gray zone of Fig. 4. In fact, it was demonstrated in Ref. [14] (reactor operating in the red zone of Fig. 4) that numerical calculation are required to extract the kinetic parameters due to the presence of mass transfer effects, which make very inaccurate the use of simple analytical solutions. Therefore, the applicability of the model strongly depends on the operating conditions: both $Pe < 1$ and $Da_{II} < 1$ have to be satisfied in the case proposed here.

5. Conclusions

This work proposes a simple method to determine the intrinsic kinetic constant of photocatalytic reactions. The procedure involves
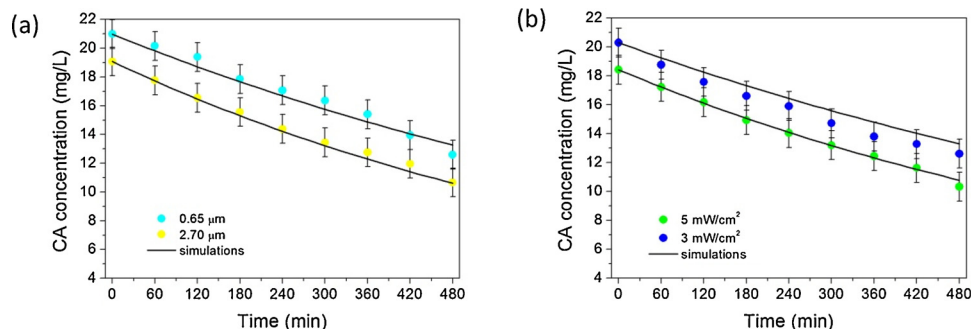

Fig. 9. Degradation of CA as a function of the irradiation time in a conventional reactor, where symbols are experimental data and full lines are the predictions of Eq. (19). (**a**) Different film thicknesses, same incident radiation (5 mW/cm^2). (**b**) Different irradiation fluxes, same film thickness (1.7 µm).

experimental runs on a photo-microreactor. Conversion data are then analyzed by using an analytical model for chemically controlled reactions and explicitly includes the radiation absorption effect. To prove the validity of the proposal, the resulting kinetics was verified against data of the same system measured in a lab-scale photo-reactor operated in the perfect mixing regime, achieving a notable prediction of its performance. In this context of results, the following concluding remarks can be outlined:

- The successful cross check of results from micro- and macro-reactors makes evident that the right formulation of the kinetic-transport model coupled to the irradiation model, as well as the operation of the reactor under suitable conditions, ensures a satisfactory rationalization of the photocatalytic problem.
- The above conditions imply that the geometry of the reaction cell needs to be properly designed, and that experiments must be run under flow conditions that satisfy the requirements of negligible mass transport limitations and uniform irradiation.
- The microreactor is easy to operate and allows one to avoid the usually expensive, time and reagent-consuming experiments in conventional reactors. The design also enables the exchange of different catalyst films on the same device, which is highly desirable for kinetic studies and catalyst screening.
- The data processing involves a straightforward linear analysis and thus avoids the implementation of demanding numerical simulations. Actually, the proposed strategy exploits all the advantages of microfluidics to accurately determine intrinsic kinetic constants. First order reactions were explored in this work, but other reaction rates can also be implemented in the calculations.
- Finally, even though improvements can still be made, the proposed method constitutes a practical tool for laboratories dedicated to modeling, design and optimization of photocatalytic reactors for environmental applications.

Acknowledgements

References

[1] N. Wang, X. Zhang, Y. Wang, W. Yu, H.L.W. Chan, Microfluidic reactors for photocatalytic water purification, Lab Chip 14 (2014) 1074–1082.

[2] R. Salgado, A. Oehmen, G. Carvalho, J. Noronha, M. Reis, Biodegradation of clofibric acid and identification of its metabolites, J. Hazard. Mater. 241–242 (2012) 182–189.

[3] P. Chen, F. Wang, Q. Zhang, Y. Su, L. Shen, K. Yao, Z. Chen, Y. Liu, Z. Cai, W. Lv, G. Liu, Photocatalytic degradation of clofibric acid by g-C_3N_4/P25 composites under simulated sunlight irradiation: the significant effects of reactive species, Chemosphere 172 (2017) 193–200.

[4] J. Madureira, E. Ceriani, N. Pinhao, E. Marotta, R. Melo, S. Cabo Verde, C. Paradisi, F.M.A. Margaça, Oxidation of clofibric acid in aqueous solution using a non-thermal plasma discharge or gamma radiation, Chemosphere 187 (2017) 395–403.

[5] T. Doll, F. Frimmel, Kinetic study of photocatalytic degradation of carbamazepine, clofibric acid, iomeprol and iopromide assisted by different TiO_2 materials-determination of intermediates and reaction pathways, Water Res. 38 (2004) 955–964.

[6] T. Doll, F. Frimmel, Photocatalytic degradation of carbamazepine, clofibric acid and iomeprol with P25 and Hombikat UV100 in the presence of natural organic matter (NOM) and other organic water constituents, Water Res. 39 (2005) 403–411.

[7] A. Manassero, M.L. Satuf, O.M. Alfano, Kinetic modeling of the photocatalytic degradation of clofibric acid in a slurry reactor, Environ. Sci. Pollut. Res. 22 (2015) 926–937.

[8] A. Visan, D. Rafieian, W. Ogieglo, R.G.H. Lammertink, Modeling intrinsic kinetics in immobilized photocatalytic microreactors, Appl. Catal. B: Environ. 150–151 (2014) 93–100.

[9] J. Parmar, S. Jang, L. Soler, D. Kim, S. Sánchez, Nano-photocatalysts in microfluidics, energy conversion and environmental applications, Lab Chip 15 (2015) 2352–2356.

[10] Z. He, Y. Li, Q. Zhang, H. Wang, Capillary microchannel-based microreactors with highly durable ZnO/TiO_2 nanorod arrays for rapid, high efficiency and continuous-flow photocatalysis, Appl. Catal. B: Environ. 93 (2010) 376–382.

[11] Z. Zhang, H. Wu, Y. Yuan, Y. Fang, L. Jin, Development of a novel capillary array photocatalytic reactor and application for degradation of azo dye, Chem. Eng. J. 184 (2012) 9–15.

[12] C. Shen, Y.J. Wang, J.H. Xu, G.S. Luo, Glass capillaries with TiO_2 supported on inner wall as microchannel reactors, Chem. Eng. J. 277 (2015) 48–55.

[13] Y. Matsushita, N. Ohba, S. Kumada, K. Sakeda, T. Suzuki, T. Ichimura, Photocatalytic reactions in microreactors, Chem. Eng. J. 135 (2008) S303–S308.

[14] G. Charles, T. Roques-Carmes, N. Becheikh, L. Falk, J.-M. Commenge, S. Corbel, Determination of kinetic constants of a photocatalytic reaction in micro-channel reactors in the presence of mass-transfer limitation and axial dispersion, J. Photochem. Photobiol. A: Chem. 223 (2011) 202–211.

[15] S. Corbel, G. Charles, N. Becheikh, T. Roques-Carmes, O. Zahraa, Modelling and design of microchannel reactor for photocatalysis, Virtual Phys. Prototyp. 7 (2012) 203–209.

[16] R. Gorges, S. Meyer, G. Kreisel, Photocatalysis in microreactors, J. Photochem. Photobiol. A: Chem. 167 (2004) 95–99.

[17] G. Takei, T. Kitamori, H.B. Kim, Photocatalytic redox-combined synthesis of L-pipecolinic acid with a titania-modified microchannel chip, Catal. Commun. 6 (2005) 357–360.

[18] H. Lindstrom, R. Wootton, A. Iles, High surface area titania photocatalytic microfluidic reactors, AIChE J. 53 (2007) 695–702.

[19] M. Krivec, A. Pohar, B. Likozar, G. Drazic, Hydrodynamics, mass transfer, and photocatalytic phenol selective oxidation reaction kinetics in a fixed TiO_2 microreactor, AIChE J. 61 (2015) 572–581.

[20] H. Eskandarloo, A. Badiei, M.A. Behnajady, G.M. Ziarani, UV-LEDs assisted preparation of silver deposited TiO_2 catalyst bed inside microchannels as a high efficiency microphotoreactor for cleaning polluted water, Chem. Eng. J. 270 (2015) 158–167.

[21] L. Lei, N. Wang, X.M. Zhang, Q.D. Tai, D.P. Tsai, H.L.W. Chan, Optofluidic planar reactors for photocatalytic water treatment using solar energy, Biomicrofluidics 4 (2010) 043004.

[22] N. Wang, X.M. Zhang, B.L. Chen, W.Z. Song, N.Y. Chan, H.L.W. Chan, Microfluidic photoelectrocatalytic reactors for water purification with an integrated visible-light source, Lab Chip 12 (2012) 3983–3990.

[23] S. Das, C. Srivastava, Microfluidic-based photocatalytic microreactor for environmental application: a review of fabrication substrates and techniques, and operating parameters, Photochem. Photobiol. Sci. 15 (2016) 714–730.

[24] A. Manassero, S.M. Zacarías, M.L. Satuf, O.M. Alfano, Intrinsic kinetics of clofibric acid photocatalytic degradation in a fixed-film reactor, Chem. Eng. J. 283 (2016) 1384–1391.

[25] D. Rafieian, R.T. Driessen, W. Ogieglo, R.G.H. Lammertink, Intrinsic photocatalytic assessment of reactively sputtered TiO_2 films, ACS Appl. Mater. Interfaces 7 (2015) 8727–8732.

[26] N. Padoin, L. Andrade, J. Angelo, A. Mendes, R.F. Peralta Muniz Moreira, C. Soares, Intensification of photocatalytic pollutant abatement in microchannel reactor using TiO_2 and TiO_2-graphene, Aiche J. 62 (2016) 2794–2802.

[27] R. Van Grieken, J. Marugán, C. Sordo, C. Pablos, Comparison of the photocatalytic disinfection of E. coli suspensions in slurry, wall and fixed bed reactors, Catal. Today 144 (2009) 48–54.

[28] N.B. Jackson, C.M. Wang, Z. Luo, J. Schwitzgebel, J.G. Ekerdt, J.R. Brock, A. Heller, Attachment of TiO_2 powders to hollow glass microbeads: activity of the TiO_2-coated beads in the photoassisted oxidation of ethanol to acetaldehyde, J. Electrochem. Soc. 138 (1991) 3660–3664.

[29] S.M. Zacarías, M.L. Satuf, M.C. Vaccari, O.M. Alfano, Efficiency evaluation of different TiO_2 coatings on the photocatalytic inactivation of airborne bacterial spores, Ind. Eng. Chem. Res. 51 (2012) 13599–13608.

[30] M. Motegh, J. Cen, P.W. Appel, J.R. van Ommen, M.T. Kreutzer, Photocatalytic-reactor efficiencies and simplified expressions to assess their relevance in kinetic experiments, Chem. Eng. J. 207–208 (2010) 607–615.

[31] O.M. Alfano, M.I. Cabrera, A.E. Cassano, Photocatalytic reactions involving hydroxyl radical attack, J. Catal. 172 (1997) 370–379.

[32] M.L. Satuf, R.J. Brandi, A.E. Cassano, O.M. Alfano, Photocatalytic degradation of 4-chlorophenol: a kinetic study, Appl. Catal. B: Environ. 82 (2008) 37–49.

[33] R. Niesner, A. Heintz, Diffusion coefficients of aromatics in aqueous solution, J. Chem. Eng. Data 45 (2000) 1121–1124.

[34] N. Padoin, C. Soares, An explicit correlation for optimal TiO_2 film thickness in immobilized photocatalytic reaction systems, Chem. Eng. J. 310 (2017) 381–388.

[35] N. Kockmann, Transport Phenomena in Micro Process Engineering, Springer, Berlin, 2008.

[36] T. Aillet, K. Loubière, L. Prat, O. Dechy-Cabaret, Impact of the diffusion limitation in microphotoreactors, AIChE J. 61 (2015) 1284–1299.

[37] T.M. Squires, R.J. Messinger, S.R. Manalis, Making it stick: convection, reaction and diffusion in surface-based biosensors, Nat. Biotechnol. 26 (2008) 417–426.

[38] T. Gervais, K.F. Jensen, Mass transport and surface reactions in microfluidic systems, Chem. Eng. Sci. 61 (2006) 1102–1121.

[39] D. Chen, F. Li, A.K. Ray, External and internal mass transfer effect on photocatalytic degradation, Catal. Today 66 (2001) 475–485.

[40] A. Aguirre, P.A. Kler, C.L.A. Berli, S.E. Collins, Design and operational limits of an ATR-FTIR spectroscopic microreactor for investigating reactions at liquid–solid interface, Chem. Eng. J. 243 (2014) 197–206.

[41] R. Hansen, H. Bruus, T.H. Callisen, O. Hassager, Transient convection, diffusion, and adsorption in surface-based biosensors, Langmuir 28 (2012) 7557–7563.

[42] R. Siegel, J. Howell, Thermal Radiation Heat Transfer, 4th ed., Taylor and Francis, New York, 2002.